



# Synthesized polymeric nanocomposites with enhanced optical and electrical properties based on gold nanoparticles for optoelectronic applications

A. Y. Yassin<sup>1,\*</sup>

<sup>1</sup> Department of Basic Sciences, Delta University for Science & Technology, Gamassa, Egypt

Received: 19 April 2022

Accepted: 31 October 2022

Published online:  
9 January 2023

© The Author(s) 2023

## ABSTRACT

In the present work, gold nanoparticles (Au-NPs) were synthesized in two ways: plant extract and laser ablation techniques. Then, Au-NPs were added to (PVP/PVA/CMC) blend (TB) to produce novel nanocomposites using the solution casting technique. X-ray diffraction analysis, Ultraviolet and visible spectroscopy, and transmission electron microscopy provided conclusive evidence for preparing Au-NPs through the above methods. The optical, structural, and dielectric properties of the prepared samples were prudently investigated and confirmed their semicrystalline nature. TEM study concluded that Au-NPs are more uniformly distributed in the TB/AuNPs-biosynthesized (TBAu-B) matrix than in the TB/Au-NPs prepared by laser ablation (TBAu-L) matrix. The decrease in interatomic distances increases the refractive index with an enhancement in optical properties. The change in loss tangent provided a deeper discernment into the relaxation dynamics that arose inside the current films. The electric modulus formalism verified the non-Debye behavior of charge carriers inside the TB-based nanocomposite samples. It also demonstrated a remarkable capacitive feature of the nanocomposite films. The dielectric characteristics of the TBAu-B nanocomposite sample have improved, where AC electrical conductivity reached  $1.58 \times 10^{-3}$  S/cm. Because of this favorable enhancement, the TBAu-B nanocomposite has the potential to be utilized in optoelectronic applications such as sensors.

## 1 Introduction

From the beginning of the twenty-first century to the present, interest in noble metal nanoparticles (MNPs) has increased among researchers, as it is an active area of both academic and industrial research [1, 2].

The frequent use of NPs has been increased over traditional fillers because of their highly demanded features. For example, researchers have paid particular attention to gold nanoparticles (Au-NPs) because of their remarkable advantages, such as non-toxicity,

Address correspondence to E-mail: a\_yassin2200@yahoo.com

high surface area, stability for a long time, and ability to interact with light. Additionally, Au-NPs are characterized by the phenomenon of surface plasmon resonance (SPR) and their size-dependent optical properties [3, 4]. These multiple properties pave the way to use and exploit them in potential technological applications, especially in energy storage devices and solar cells [5]. Its uses also extend to drug delivery, anticorrosion, imaging, and detection of biomolecules, including DNA and proteins [4, 6, 7].

The polymer blending method is one of the simplest and most effective techniques for designing new compounds with superior physicochemical properties for a specific application. Poly (vinyl pyrrolidone) and poly (vinyl alcohol), symbolized by PVA and PVP, respectively, are polar hydrophilic polymers. Both are biocompatible, flexible, and moderate in their optical, thermal, and electrical properties [8, 9]. PVP/PVA blends have attracted the attention of many researchers who have made much effort to obtain new and high-efficiency compounds [2, 10–15]. Their use extends to biological, pharmaceutical, and engineering fields. Deghiedy and El-Sayed [16] studied the structural and optical properties of the PVA/PVP blend after exposing it to gamma radiation. The irradiated films showed an improvement in their optical properties. In comparison, Veena and Lobo [17] are interested in investigating the thermal properties of the PVA/PVP blend filled with potassium permanganate ( $\text{KMnO}_4$ ). They reported that the structural changes due to adding the filler affected the crystallinity of the prepared samples.

Despite all the efforts, the challenge remains to tailor advanced functional materials with high dielectric properties that retain stored energy for a long time without leaks, saving in increased cost and complicated preparation steps. So, sodium carboxymethyl cellulose (CMC) polymer was chosen to prepare a ternary blend. CMC polymer is derived from cellulose and has several desirable properties, including non-toxicity, recycling, easy availability, biocompatibility, and eco-friendly behavior [18, 19]. Moreover, films formed using CMC are characterized by high transparency and mechanical strength, which are recommended for use in various commercial applications, such as, textiles, varnishes, paints, medicines, food, and makeup.

Although some published articles have been concerned with studying the importance of surface

plasmons for AuNPs and how to benefit from this important feature in applications, few have examined the dielectric properties of AuNPs-based composites. Various methodologies are also used to synthesize Au-NPs, including pulsed laser ablation, chemical routes, irradiation, and plant extracts. No evident study was interested in comparing the production efficiency of Au-NPs from these techniques and their effect on optical, morphological, and electrical properties.

Therefore, this work covered this research point and found the best preparatory methods characterized by simplicity, low cost, and achieving a high dielectric constant of the prepared compound, where controlled materials' physical and chemical properties are essential in their functionalities. It is also useful in reducing the use of chemicals harmful to the environment and negatively affecting human health.

Herein, various properties of the AuNPs-filled TB nanocomposites were deeply studied, such as structural investigation using FT-IR and XRD. At the same time, optical and morphological characteristics were scrutinized via UV-Vis, SEM, and TEM, respectively. Besides, these samples' conduction mechanism, charge carriers' relaxation performance, and dielectric findings have been systematically interpreted. These investigations provided a deep insight into the influential role of Au-NPs synthesized in two different ways in enhancing their structural, optical, and electrical properties. They will also benefit from employing the final product in optoelectronic applications with the best features.

## 2 Experimental work

### 2.1 Materials

PVP bought from SISCO Research Lab. Ltd. (India) has a molecular weight (MW)  $\approx$  of  $40 \times 10^3 \text{ g mol}^{-1}$ . PVA was purchased from E-Merck (Germany) with MW  $\approx 14 \times 10^3 \text{ g mol}^{-1}$ . These compounds are branded owing to their high analytical degree. CMC (MW  $\approx 90 \times 10^3 \text{ g mol}^{-1}$ ) and Chloroauric acid ( $\text{HAuCl}_4$ ) bought from Sigma-Aldrich were sagaciously used without any additional refinement. All chemicals are of 99.5% purity.

## 2.2 Preparation of leaves' extract

Leaves of *Hamelia patens* were carefully rinsed many times with double distilled water (DD) and left for four days to be dry in the dark. Twenty-five grams of the collected powder was boiled in DD water with a ratio of 1:10 for 50 min. The final extract was filtered and then stored at 4 °C in a refrigerator for later use.

## 2.3 Bio-synthesis of AuNPs

2 ml of leaf extract was dispersed into 150 ml of  $\text{HAuCl}_4$  solution (1 mM/ml) with 20 min of stirring. As exhibited in Fig. 1a, the addition of faintly yellowish  $\text{HAuCl}_4$  to the leaf extract (which is a pale brown) produced a pink color, indicating the successful synthesis of Au nanoparticles.

## 2.4 Synthesis of AuNPs using the laser ablation technique

The detailed preparation steps for Au nanoparticles are presented in Fig. 1b and reported in our previous article [4]. In brief, a bulk of gold previously cleaned using DD water and chlorobenzene with suitable dimensions  $0.4 \times 0.4 \times 0.1$  (cm) has been used as a target for preparing AuNPs. A laser beam with a 1064 nm primary wavelength has been produced from Nd:YAG nanosecond pulsed laser and perpendicularly incident on the gold target, placed in 30 ml

DD water. The gold has been smashed into tiny nanometer-sized pieces.

## 2.5 Preparation of (PVP/CMC/PVA)/AuNPs samples

PVP powder (3 g) dissolved completely with DD water (150 ml). Similar procedures were done separately with three grams of PVA and CMC. The three solutions were vigorously stirred for 2.5 h at a temperature of 65 °C. PVP/PVA and PVP/PVA/CMC blends were synthesized by mixing equal amounts of these solutions. Au-NPs nanofillers prepared in two ways were added to the PVP/CMC/PVA blends. Then, Petri dishes were accurately cleaned, and the homogeneous mixtures were prudently dropped onto them. The present system was dried for 72 h at 50 °C in a vacuumed oven.

The PVP/PVA binary blend and PVP/PVA/CMC ternary blend were denoted as BB and TB, respectively. TBAu-L represented the PVP/PVA/CMC/Au-laser nanocomposite, whereas TBAu-B represented the PVP/PVA/CMC/Au-biosynthesized nanocomposite.

## 2.6 Characterization

Structural properties of the prepared films have been studied by using a high-resolution X'Pert PRO MRD X-ray Diffractometer (PANalytical) at 293 K with Cu-

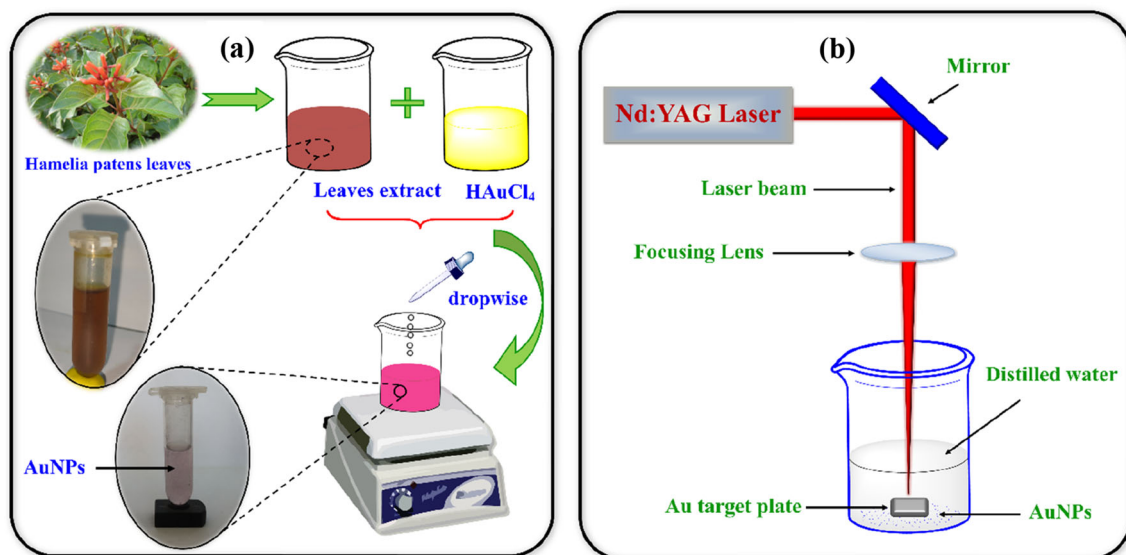


**Fig. 1** Preparation steps of gold nanoparticles by **a** leaves extract, and **b** laser ablation technique

$K\alpha$  radiation, where Bragg's angles ( $2\theta$ ) were ranged from  $3^\circ$  to  $70^\circ$ .

Utilizing a double beam spectrophotometer, a UV-Vis spectroscopic study of the previously produced samples was performed in the wavelength range from 190 to 1100 nm. The spectrophotometer is of JASCO model V/670 ~ UV-Vis/NIR. The Nicolet *iS-10* attenuated total reflectance-Fourier transforms infrared (ATR-FT-IR) spectrophotometer was employed to investigate the chemical structure of the prepared films. The ATR-FT-IR spectral analysis was carried out in the range of  $4000$  to  $500\text{ cm}^{-1}$ . The changes in surface morphology were deeply studied via JEOL JSM 6510 LV scanning electron microscope (SEM) (United States of America) and operated at  $20 \times 10^3\text{ V}$ . The prepared samples were put onto carbon-coated copper grids ( $\sim 200$  mesh), and they were analyzed using HRTEM operating at 200 kV. It is a JEOL JEM-2100 model (Japan). The present system's dielectric and dynamic relaxation responses were studied using the broadband dielectric spectrometer (BDS Turnkey) (concept 40) in the frequency range of (0.1–20 M) Hz. This apparatus is characterized by its highly reliable data using the Novo control system with a parallel-plate capacitor and two gold-plated electrodes, in addition to the QUATRO Cryo system, which helps maintain temperatures within  $\pm 0.01\text{ }^\circ\text{C}$ .

### 3 Results and discussion

#### 3.1 XRD analysis

XRD studies are often performed because of their essential role in elucidating microstructural changes in polymeric materials. Therefore, it was utilized to confirm whether amorphous or crystalline areas predominated within the (PVP/PVA/CMC)/Au nanocomposite films, and to evaluate the impact of Au-NPs on the structural features of these nanocomposites.

XRD characteristic patterns demonstrated in Fig. 2 for the BB, TB, and the TB blend filled with AuNPs are characterized by a broad peak at  $2\theta \approx 19.41^\circ$ , confirming the semicrystalline nature of the TB-based nanocomposites. This peak is attributed to BB with (110) reflective plane [8], which shifted to  $\approx 19.71^\circ$  due to the incorporation of CMC into the PVP/PVA blend.

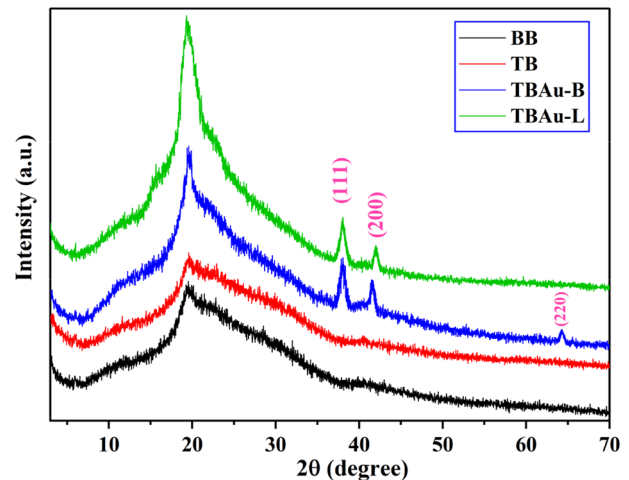


**Fig. 2** XRD characteristic patterns of the BB, TB, and the TB/Au-NPs nanocomposites

The addition of AuNPs boosted the strength of this broad peak, indicating an increase in the number of crystalline regions within the host TB matrix. It is noteworthy that the nanocomposite sample containing biosynthesized AuNPs attained a slight increase in intensity compared to the nanocomposite with the prepared AuNPs by Laser ablation, which enhances the applicability of the TBAu-B nanocomposite in the field of energy storage.

New sharp diffraction peaks observed at  $2\theta = 37.91^\circ$  (111),  $42.12^\circ$  (200), and  $64.29^\circ$  (220) were ascribed to AuNPs, which are consistency with data documented in the standard card (JC-PDS file No. 4-0784), signifying the successful synthesis of Au-NPs [4]. The appearance of such changes is evidence of the compatibility and effective complexation of the AuNPs with the TB host material.

The Debye-Scherrer equation was used to calculate the average crystallite size ( $D_{cr}$ ) through the following formula [20]:

$$W_{hm} = \frac{0.94\lambda}{D_{cr}\cos\theta_m}, \quad (1)$$

where  $\theta_m$  is the Bragg's angle,  $W_{hm}$  is the full width at half peak maximum of the diffraction angle  $\theta_m$ , and  $\lambda$  is the wavelength of the incident radiation ( $\lambda = 1.54056\text{ \AA}$ ).

Further, the Williamson-Hall equation [21] was used to calculate the crystallite size and average lattice strain:

$$W = W_{strain} + W_{hm} = 4\epsilon \tan \theta_m + \frac{0.94\lambda}{D_{cr} \cos \theta_m}, \tag{2}$$

where  $W$  is the full width at half maximum of the XRD peaks and  $W_{strain}$  is the strain broadening which is uniform in all crystallographic directions. Multiplying Eq. (2) by  $\cos \theta_m$  yields

$$W \cos \theta_m = 4\epsilon \sin \theta_m + \frac{0.94\lambda}{D_{cr}} \tag{3}$$

By studying the relation between  $W \cos \theta_m$  and  $4 \sin \theta_m$ , the  $D_{cr}$  values and the strain ( $\epsilon$ ) were determined for the synthesized samples.

In addition to Debye–Scherrer’s and Williamson–Hall’s (WH) equations, other approaches can be used to estimate the value of crystalline size and micro-strain, i.e., Halder–Wagner (HW) and size-strain plot (SSP) techniques [22]. Table 1 shows the calculated value of crystalline size and micro-strain of the nanocomposite samples filled with Au-NPs at room temperature. All  $D_{cr}$  values calculated using Williamson–Hall, Halder–Wagner, and SSP techniques are greater than those determined by the Debye–Scherrer equation since these techniques represent all diffraction peaks and lattice strain, while the Scherrer equation does not [22].

### 3.2 Surface morphological features

SEM examination was used to investigate the influence of incorporating AuNPs on the morphological and microstructural features of the above-described samples, as shown in Fig. 3. At a magnification of 2500 times, typical micrographs of the produced nanocomposite samples were captured. No phase separations were identified in this figure, indicating that the TB polymeric blend is compatible with AuNPs. The nanocomposite micrographs exhibited rough morphology compared to the pure blend micrograph displayed in Fig. 3a, distinguished by its smooth surface. The SEM images in Fig. 3c–d show brilliant protruding microparticles distributed consistently across their surfaces. Figure 3d of the TBAu-

L nanocomposite has a much rougher surface than Fig. 3c of the TBAu-B nanocomposite, promoting the sample containing Au prepared using plant extraction over the sample containing Au prepared using laser ablation. Au-NPs agglomerates were identified as the source of the protruding microparticles, indicating the nanofiller’s physical interaction with the TB polymer blend.

### 3.3 TEM analysis

The transmission electron microscope (TEM) technique is usually used to determine the synthesized nanoparticles’ size, shape, and distribution. Figure 4 shows the TEM micrographs of the Au-NPs prepared in two different ways and their congruous histograms that reveal the size of the synthesized nanoparticles. This figure exhibits that the AuNPs are more uniformly distributed in the TBAu-B matrix than in the TBAu-L matrix. Further, the AuNPs shapes vary from triangular to hexagonal, irregular, and spherical. The biosynthesized AuNPs are 3–24 nm, while the size of AuNPs prepared using the laser ablation technique is 2–30 nm, emphasizing the XRD spectroscopic results.

### 3.4 FT-IR spectroscopy

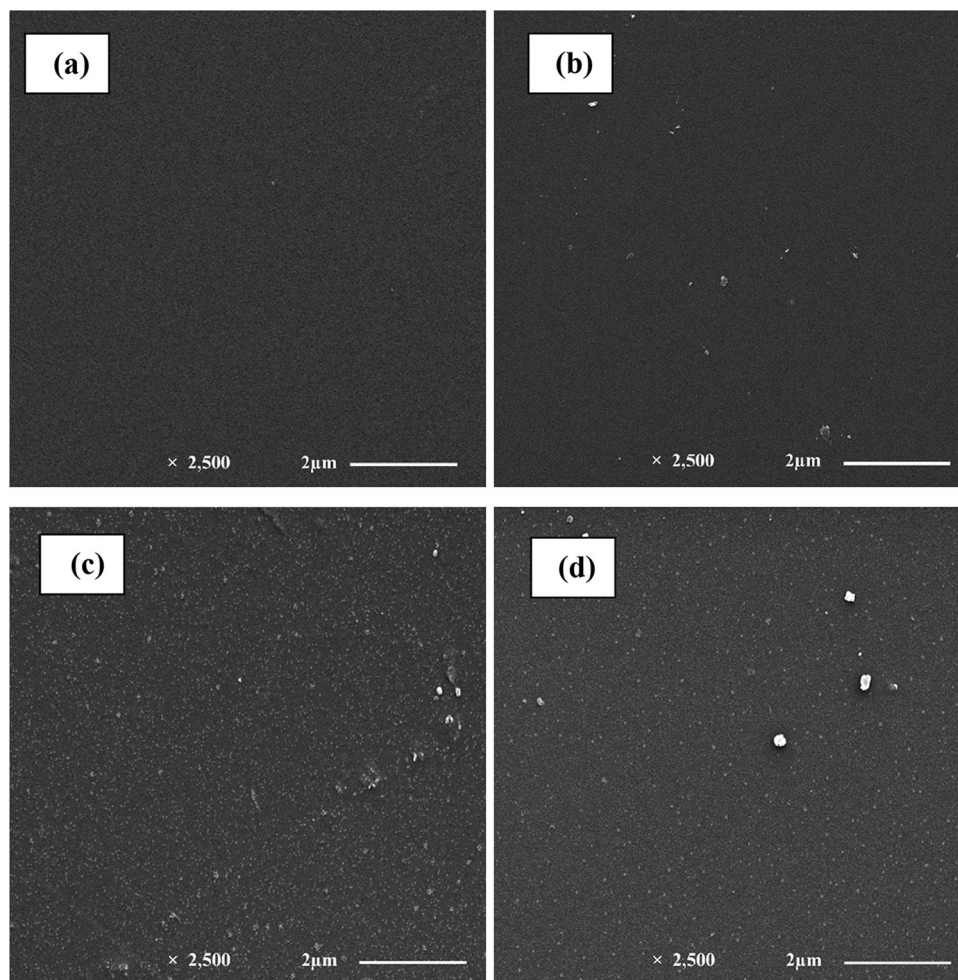
A spectroscopic investigation based on FT-IR data was applied at room temperature for BB, TB, TBAu-L, and TBAu-B prepared films, as shown in Fig. 5. The spectral charts contain some bands such as, –OH stretching (str.) functional group of CMC at  $3366 \text{ cm}^{-1}$ ,  $2936 \text{ cm}^{-1}$  (H–C–H asymmetrical str.), and  $1441 \text{ cm}^{-1}$  (–CH<sub>2</sub> scissoring). Some peaks of PVP, such as the C=N peak positioned at  $1496 \text{ cm}^{-1}$  of the pyridine ring and the peak at  $933 \text{ cm}^{-1}$ , appeared due to the –CH bending vibrational group related to out-of-plane rings [10]. More bands’ assignments for the FT-IR spectra of the prepared samples are summarized in Table 2.

Some peaks in the TBAu-L and TBAu-B spectra showed small shifts compared to the TB spectrum

**Table 1** The calculated value of crystalline size ( $D_{cr}$ ) and micro-strain ( $\epsilon$ ) of the nanocomposite samples filled with Au-NPs at room temperature

W (wt %)	Debye–Scherrer		Williamson–Hall		Halder–Wagner		SSP	
	$D_{cr}$ (nm)		$D_{cr}$	$\epsilon$	$D_{cr}$	$\epsilon$	$D_{cr}$	$\epsilon$
TBAu-B	27.28		38.2	0.84	36.66	0.56	35.9	0.54
TBAu-L	29.48		39.6	2.3	39.01	1.35	40.2	1.24

**Fig. 3** The SEM micrographs of **a** BB blend, **b** TB blend, **c** TBAu-B, and **d** TBAu-L samples at magnification 2500 times



due to the filling of the TB matrices with AuNPs. For example, the  $3366\text{ cm}^{-1}$  band has shifted toward a lower wavenumber to  $3333\text{ cm}^{-1}$  due to the addition of biosynthesized AuNPs. Additionally, the spectra showed considerable variations in the intensity of several bands as a result of the physicochemical interactions, with the TB matrices acting as electron donors and the AuNPs acting as electron acceptors [3, 23].

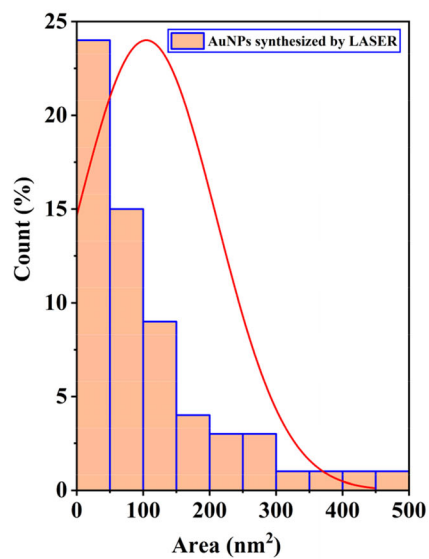
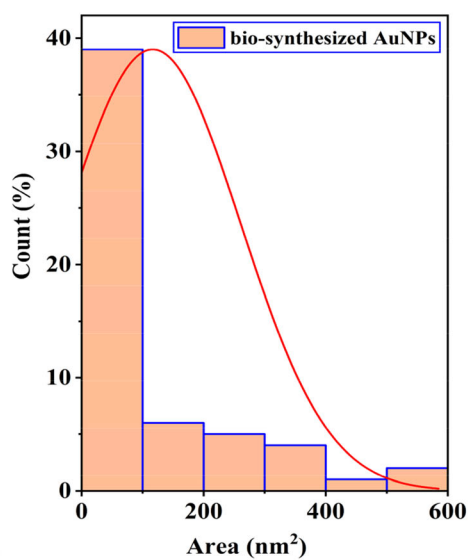
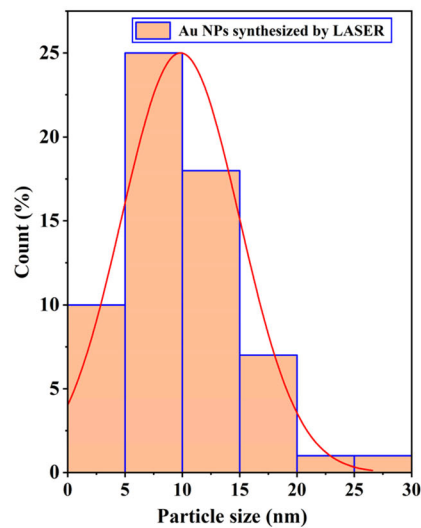
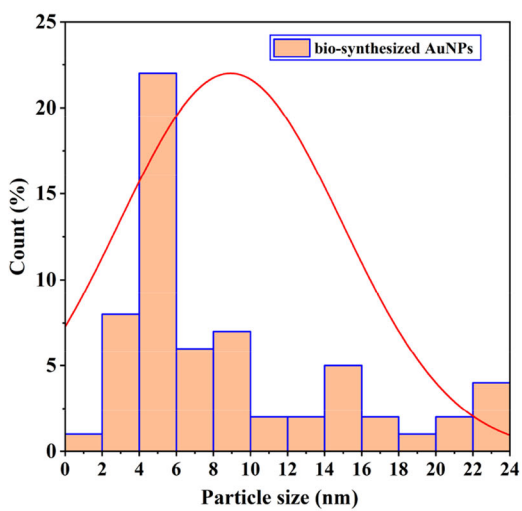
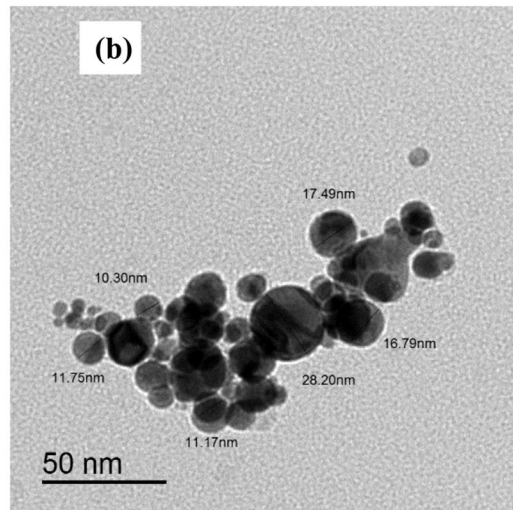
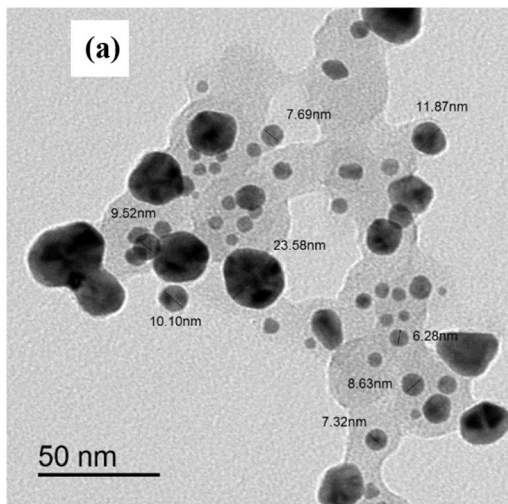
The presence of oxygen in the ether linkage enables intermolecular hydrogen interactions with various molecules in the PVP and CMC polymers. The outcome was forming a high-intensity peak at  $1094\text{ cm}^{-1}$  [24]. This peak confirms the semicrystalline structure of the current nanocomposite samples.

Further, the two spectral bands observed at  $1559\text{ cm}^{-1}$  and around  $1319\text{ cm}^{-1}$  are attributed to intra-molecular interaction of the asymmetric carboxylate ( $-\text{COO}^-$ ) str. groups with the bending hydroxyl groups ( $-\text{OH}$ ). The presence of such two

functional groups plays an influential role in increasing the possibility of complexing between the Au-NPs and the TB blend [25], which enhances the structural properties of their nanocomposites and affirms the preceding results.

### 3.5 Ultraviolet and visible analysis

UV-Vis spectroscopy was exploited to elucidate the influence of the interaction of AuNPs synthesized in two different ways with the TB blend on the optical behavior of the produced films. Figure 6 demonstrates the UV-Vis absorption spectra of BB, TB, and AuNPs-based nanocomposites in the wavelength region from 190 to 1100 nm recorded at room temperature. The UV spectrum's characteristic sharp absorption edge showed at around 238 nm for BB and 246 nm for the TB blend. The noticeable difference in the height of this edge between the TBAu-B and TBAu-L samples is attributed to the disorder



◀ **Fig. 4** The TEM micrographs of the AuNPs prepared in two different ways and their corresponding histograms related to the nanoparticles size distribution and their areas

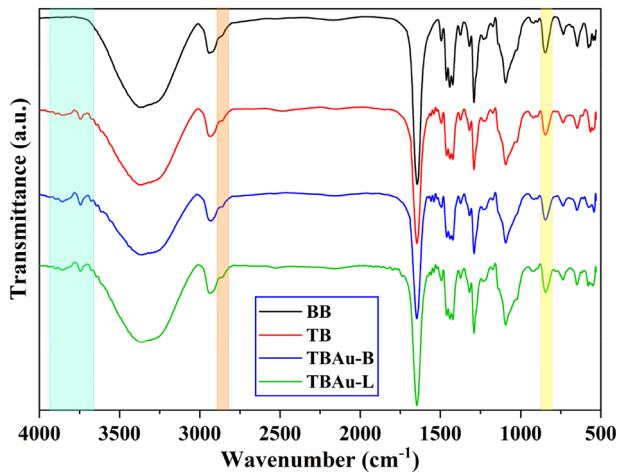


**Fig. 5** FT-IR spectral charts of the blends with and without AuNPs

caused by AuNPs populating the host matrices. In another expression, this change is due to the widespread amorphous areas within the TB matrix besides some crystalline regions, confirming XRD results, i.e., the semicrystalline nature of the nanocomposite samples. Also, the bathochromic (red) shift observed in the position of this edge from 246 to 260 nm leaves no doubt about the successful complexation between the aforementioned nanocomposites' constituents.

Electronic transitions from HOMO to LUMO are the main reason for charge transfer absorption bands. Thus, the band localized at  $\approx 225$  nm is assigned to  $n \rightarrow \pi^*$  transition [28], which was blue-shifted toward 220 nm. This shift, in turn, asserts the strong

**Table 2** Bands' assignments for the FT-IR spectra of the prepared samples under study

Wavenumber ( $\text{cm}^{-1}$ )	Band assignment	source	Ref
3366	–OH str	CMC	[15]
2936	H–C–H asymmetrical str	CMC	[15]
1641	C=O str	CMC	[15]
1441	–CH <sub>2</sub> scissoring	CMC	[26]
850	–CH rocking	PVA	[10]
1293	–CN str	PVP	[10, 26]
1496	C=N of pyridine ring	PVP	[8]
933	–CH bending (out-of-plane rings)	PVP	[10]
2868	CH <sub>2</sub> symmetrical str. (shoulder)	PVA	[8, 25]
1024	C–O str. (shoulder)	PVA	[27]

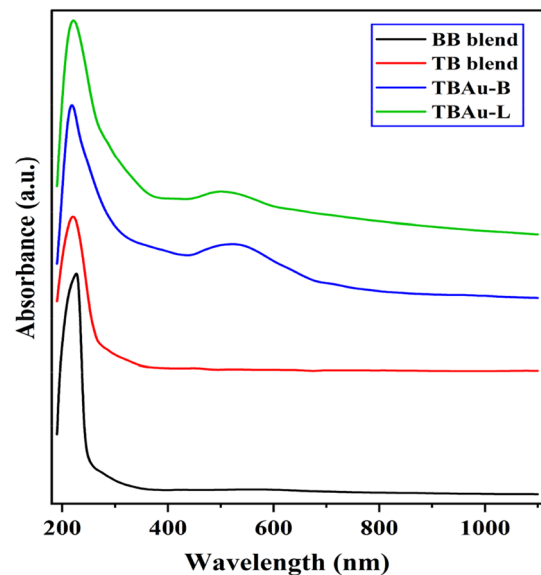


**Fig. 6** The UV–Vis absorption spectra of BB, TB, and AuNPs-based nanocomposites in the wavelength region from 190 to 1100 nm at room temperature

conjugation among the nanofiller and TB polymer blend [27], where the TB host matrix acts as reducing/capping agents on the surface of AuNPs.

The green synthesized gold nanoparticles spectrum in Fig. 7 exhibits a broad peak at 539 nm, while the broad peak observed at 531 nm is attributed to the AuNPs prepared by laser ablation. The nanocomposite spectra exhibit absorption peaks at about 525 nm for TBAu-B and 517 nm for TBAu-L, attributed to the surface plasmon resonance (SPR) phenomenon of AuNPs [29]. Therefore, this peak verifies the successful synthesis of AuNPs by extraction from the *Hamelia patens* and using the laser ablation technique.

Based on the fact that the SPR is sensitive to light radiation, where free electrons of AuNPs oscillate



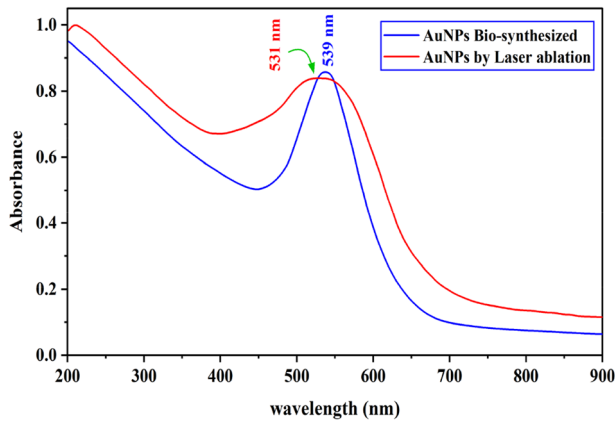


**Fig. 7** The UV–Vis absorption spectra of synthesized AuNPs by **a** leaves extract, and **b** laser ablation technique

due to their interaction with incident photons. Thus, such a peak indicates the suitability of these films, which are flexible enough to be employed in biomedical devices and optoelectronic applications such as photosensors. Further, the blue shift of SPR peaks (from 539 to 525 nm for TBAu-B and from 531 to 517 nm for TBAu-L) stemmed from the quantum confinement effect, which implies the decrease in AuNPs size.

### 3.5.1 Optical constants

**3.5.1.1 Optical energy gap ( $E_g$ )** Additional studies on optical absorption in UV–Vis regions were carried out to verify the applicability of the nanocomposite samples in optoelectronic applications. Commonly, transitions that could occur at the absorption edge of polymeric composites have two different kinds; indirect and direct transitions [30–33]. Tauc’s plot is based on Eqs. (4) and (5) [8], where  $(\alpha h\nu)^2$  and  $(\alpha h\nu)^{1/2}$  were plotted as functions of energy ( $h\nu$ ) in Fig. 8 to determine the direct ( $E_{gd}$ ) and indirect ( $E_{gi}$ ) optical energy gaps, respectively.

$$(\alpha h\nu)^2 = F_1(h\nu - E_{gd}) \tag{4}$$

$$(\alpha h\nu)^{\frac{1}{2}} = F_2(h\nu - E_{gi}), \tag{5}$$

where  $h\nu$  represents the energy of incident photons,  $\alpha$  is the absorption coefficient, and  $F_1$  and  $F_2$  are constants. The absorption coefficient was calculated by knowing the absorbance (Abs) and the thickness ( $d$ ) of the sample under study as represented in the following formula [34]:

$$\alpha(\nu) = 2.303 \times \frac{Abs}{d} \tag{6}$$

The calculated direct and indirect optical band gaps of the above-described samples are summarized in Table 3. From the obtained values, it is clear that the incorporation of AuNPs led to a significant decrease in the  $E_g$  values, where the TBAu-B nanocomposite is promoted over the TBAu-L nanocomposite by attaining the lowest  $E_g$  value. This decrease originated from the numerous polaronic contributions and imperfections within the TB-based nanocomposites. Furthermore, the charge carriers tend to move from the lower energy level to the higher energy level to the indirect transfer because this path needs a small amount of energy to be carried out. In contrast, the direct transition requires a relatively more significant amount of energy.

The exponential decay tail detected in all the curves of Fig. 8 at lower energies suggests that the localized levels formed in the band gap are ascribed to structural disorder in the host matrix [35]. Moreover, it confirms the dominance of amorphous regions within the synthesized films over the crystalline regions, confirming the results of previous measurements.

**3.5.1.2 Refractive index** The refractive index ( $n$ ) plays a very influential role in designing integrated optical devices, which primarily rely on ions’ electronic polarization [36]. The  $n$  values were determined by substituting extinction coefficient ( $k$ ) in the following equation [37], and the results are summarized in Table 3:

$$n = \frac{1 + R}{1 - R} + \sqrt{\frac{4R}{(R - 1)^2} - k^2} \tag{7}$$

$$k = \frac{\lambda\alpha}{4\pi} \tag{8}$$

The increase in nanocomposite density due to the incorporation of Au-NPs into the TB host matrix affected their light penetration velocity. It thus increased the refractive indices of the present samples. In another expression, the decrease in interatomic distances caused by the higher density inside the nanocomposites led to a rise in the coordination number. Thus, the more non-bridging oxygen bonds there are, the higher the calculated refractive index [38], suggesting that the TBAu-B and TBAu-L

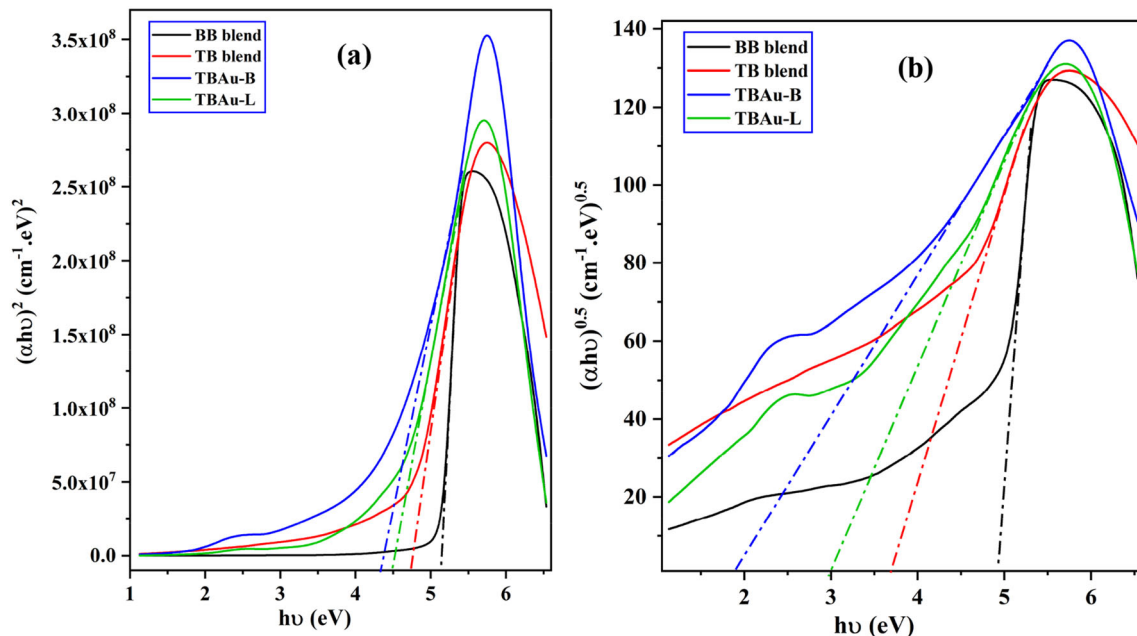


**Fig. 8** The  $(\alpha h\nu)^2$  and  $(\alpha h\nu)^{1/2}$  as functions of energy ( $h\nu$ ) for the current samples

**Table 3** Direct and indirect optical energy gap ( $E_g$ ), refractive index, and the relaxation time ( $\tau$ ) of the described composite films

W (wt %)	$E_g$ (eV)		Refractive index ( $n$ )	Relaxation time (s)
	Direct	Indirect		
BB blend	5.13	4.91	1.2	–
TB blend	4.72	3.7	1.31	$7.44 \times 10^{-3}$
TBAu-B	4.32	1.88	1.78	$5.52 \times 10^{-4}$
TBAu-L	4.5	3	1.62	$2.4 \times 10^{-4}$

nanocomposites are viable candidates for industrial applications in the optoelectronic sector.

### 3.6 Dielectric spectral analyses

#### 3.6.1 Dielectric permittivity study

Dielectric features of the BB, TB, TBAu-L, and TBAu-B prepared films were studied in the frequency range of  $1 \times 10^{-1} - 2 \times 10^7$  Hz. The complex dielectric permittivity can be defined through the following equation based on its real and imaginary parts, which are symbolized by  $\epsilon'$  and  $\epsilon''$ , respectively [39];

$$\epsilon^* = \epsilon' - j\epsilon'' = \frac{C_p d}{\epsilon_0 A_e} - j \frac{\sigma}{2\pi f \epsilon_0} \quad (9)$$

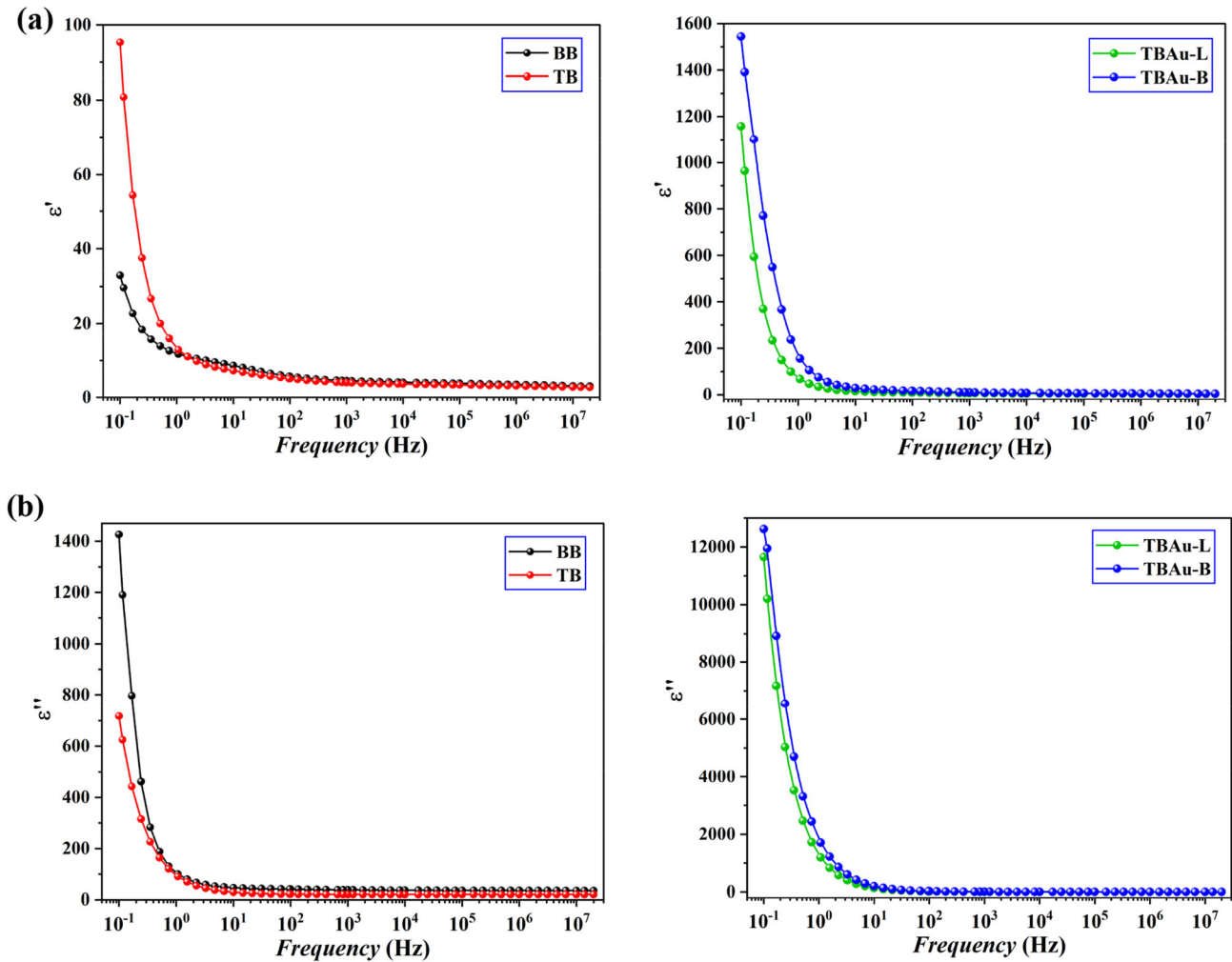
where  $C_p$  is the capacitance value, while  $A_e$  symbolizes the electrode's cross-sectional area.

Figure 9a exhibits the values of  $\epsilon'$  versus frequency ( $f$ ) over the range mentioned above, while Fig. 9b

displays the frequency dependence of  $\epsilon''$  values for all the prepared samples. The two factors are similar in their behaviors, where they attained the highest values in the low-frequency region ( $f < 30$  Hz), and their values drastically decreased with the regular increase in  $f$ -values. Obviously,  $\epsilon'$  and  $\epsilon''$  depend on the nanocomposites' constituents because their values have improved after incorporating Au-NPs into the TB matrix. Notably, the nanocomposite that contains biosynthesized AuNPs has attained the best  $\epsilon'$  value.

The success of dipoles in tracking the change of field direction had the most significant effect in achieving large values in the  $\epsilon'$  values at frequencies below 150 Hz, enhancing the interfacial polarization between the TB blend and AuNPs.

On the contrary, ionic and electronic polarization did not significantly participate in the frequency region ( $f \geq 10^2$  Hz), reducing the  $\epsilon'$  and  $\epsilon''$  values. Furthermore, this trivial variation is attributable to



**Fig. 9** The variation of frequency with **a**  $\epsilon'$  and **b**  $\epsilon''$  for the BB, TB, TBAu-B, and TBAu-L samples recorded at room temperature

the dielectric relaxation response within the TB polymeric matrices [40].

Hence, incorporating AuNPs nanofiller into the PVP/PVA/CMC blend had a beneficial impact on improving in the dielectric features of the synthesized films, precisely the TBAu-B sample, confirming the XRD and UV-Vis findings.

It is worth mentioning that the leakage of stored energy caused the slight loss of dielectric recorded due to the direct contact of the Au-NPs. Coating the gold nanoparticles with small layers of the TB blend prevents such leakage, where these layers indicate that the TB is respectably compatible with the AuNPs. The presence of Au-NPs between two TB layers, distinguished by their dielectric manner, is good evidence for the formation of micro-capacitors inside the PVP/PVA/CMC blend [39].

### 3.6.2 Dielectric relaxation response

The change in loss tangent ( $\tan \delta$ ) with frequency shown in Fig. 10 for the produced films was carefully studied at 293 K, thus providing a deeper distinction in the relaxation dynamics that arose inside the existing films.

The characteristic strong relaxation peak observed in the loss tangent figure originated from the complexation between ions and induced dipoles inside the polymer segments. Its asymmetrical shape in the low-frequency region ( $f \leq 10^{-3}$  Hz) affirms the semicrystalline structure of the (PVP/PVA/CMC)-based nanocomposites. Further, the appearance of this peak at low frequencies is assigned to the  $\alpha$ -relaxation response, which is linked with a rotating movement of functional groups dispersed at both sides of the central chain axis of the TB matrices [14].

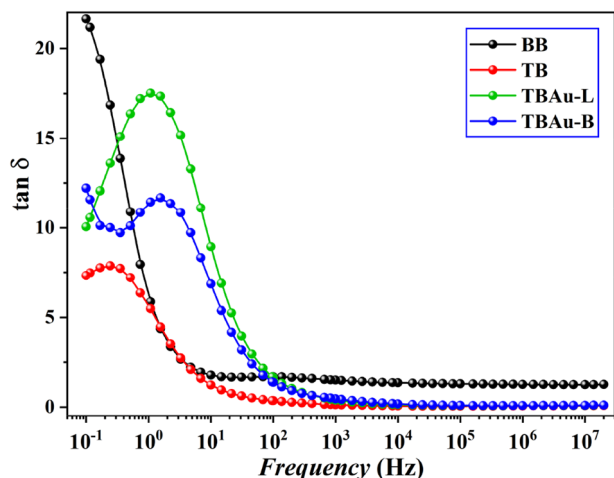


**Fig. 10** The change in loss tangent ( $\tan \delta$ ) of the pure blends and their nanocomposite films with frequency at 293 K

This finding confirms the domination of electronic conduction within the host polymeric matrix.

The first part of this peak exhibits an increase in  $\tan \delta$  with frequency in a low-frequency region. Its behavior indicates that the ohmic nature of the samples is more dominant than their capacitive nature. The sudden drop in  $\tan \delta$  values (the second part) implies that the polymer blended with Au-NPs succeeded in forming micro-capacitors, which enhances the capacitance of the existing nanocomposites [41]. The maximum value recorded for  $\tan \delta$  is 11.7 for the TBAu-B nanocomposite, while its value for the TBAu-L is 17.5. Sadiq et al. [42] reported that the maximum value of  $\tan \delta$  for PVA/PVP blend filled with 15 wt% rGO was about 12, recommending the present nanocomposite over other composites.

The apparent shift in the peak's location toward the right (high-frequency values) has resulted from new interfacial zones between the TB and AuNPs. Consequently, the decrease in free volumes inside the TB matrices reduces the relaxation times ( $\tau$ ) value. This reduction clearly indicates the uniform distribution of the AuNPs, especially in the TBAu-B nanocomposite, due to their small size, as discussed in the TEM results. This nanocomposite film significantly improved comparative advantages over other samples, giving it a priority for use in the fabrication of energy storage devices.

### 3.6.3 Electric moduli

Electric moduli analysis can suppress the effect of electrode polarization. The following formulas

govern the relationship between the real and imaginary parts of the electric modulus:

$$M' = \frac{\epsilon'}{\epsilon'^2 + \epsilon''^2} \quad (10)$$

$$M'' = \frac{\epsilon''}{\epsilon'^2 + \epsilon''^2} \quad (11)$$

Figure 11a represents the dependence of  $M'$  values on the frequency where the data were measured at room temperature. The spectra are divided into two sections: the first section in the low-frequency region has a tail shape, whereas the second section lies at medium/high frequencies and is shaped as a sigmoid.

Such a tail indicates that the electrode polarization does not influence the conduction process. The increase in the width of this tail after filling with Au-

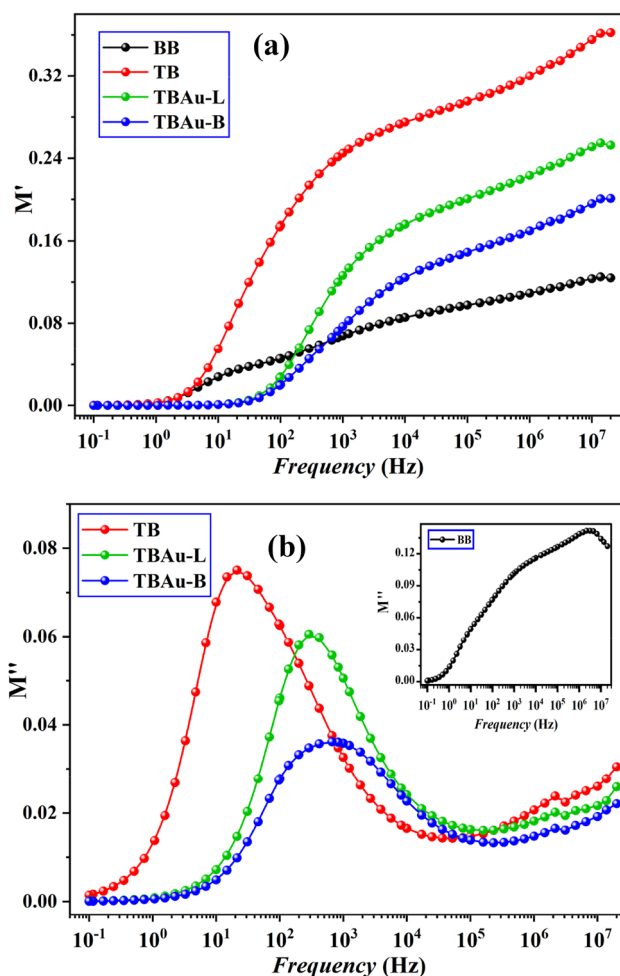


**Fig. 11** The variation of frequency with **a**  $M'$  and **b**  $M''$  for the BB, TB, TBAu-B, and TBAu-L samples recorded at room temperature

NPs denotes that the TB-based nanocomposites are of outstanding capacitive behavior [39], supporting the above findings. Also, the reduction in  $M'$  values found as a result of integrating the nanogold into the TB matrix suggests that triggered electrons hop from one place to another. This finding confirms that hopping is the dominant conduction mechanism in the current nanocomposite samples [14].

Figure 11b depicts the dependency of  $M''$  data on frequency observed at room temperature for the current samples. The characteristic peak in  $M''$  spectra clearly indicates the induced electrons' relaxation process. It is also known as the conductivity relaxation peak. Such a peak in the  $M''$  spectrum refers to the alternation in charge carriers' transition from long-range within the host polymeric matrix to short-range [43].

The  $M''$  loss peak exhibited a remarkable reduction in its intensity due to mixing the AuNPs with TB, which is of a non-Debye type [44] and is quite similar to the dielectric relaxation caused by the Maxwell–Wagner–Sillars (MWS) polarization phenomenon [15]. Then, this dramatic decrease in the  $M''$  values has followed by a gradual increase with the further increase of the frequency, which implies that another dielectric relaxation process has arisen inside these nanocomposites in the high-frequency region. The latter relaxation process at high frequency is attributed to the dipolar reorientation of some functional groups such as, N–O and -OH. Similar behavior was reported in the literature [14, 15]. The decreasing trend in relaxation times, as shown in Table 3, is due to the implementation of new interfacial sections with the addition of Au nanoparticles, through which the induced electrons can move. These results confirm that the prevailing ac conductivity is of a hopping sort and emphasize the above  $M'$  findings.

### 3.6.4 Electric modulus scaling

Scaling of  $M''$  curves versus normalized frequency ( $f/f_{max}$ ) of the TBAu-B and TBAu-L nanocomposites compared to the TB curve is depicted in Fig. 12 at room temperature. From this figure, the spectra of the above-described films have clearly collapsed onto a single master curve in the medium frequency region for TBAu-B, whereas they have superimposed at lower frequencies for TBAu-L. This behavior indicates that the relaxation dynamics do not depend on the composition of the nanocomposites [45].

Nevertheless, the spectra deviated from the typical master curve in the high-frequency region because of the confinement of charge carriers in potential wells. The observed slight deviation also implies that the relaxation process during the electrical conduction is contingent on the presence of AuNPs inside the films under study. Moreover, the asymmetric peak found in these curves confirms the non-Debye response of the nanocomposite samples [14].

The variation of  $M''$  versus  $M'$  (Cole–Cole plot representing Argand diagrams) was plotted for the synthesized samples as exhibited in Fig. 13. The Cole–Cole plot is generally divided into three frequency-dependent regions; low-, middle-, and high-frequency regions. The three regions are ascribed to the grain boundary effect, the participation of grains, and the bulk conduction relaxation process, respectively. The present spectra are characterized by a single semicircular arc attributed to the grain boundary effect and surface polarization, while the spike observed is assigned to the bulk conduction response. The asymmetrical behavior of this relaxation peak verifies the non-Debye dielectric relaxation response. The dielectric relaxation processes in the current system can be represented by a parallel combination of a resistor (R) and a geometrical capacitor (C) [46]. The following equation governs the relaxation peak frequencies:

$$f_{max} \approx \frac{1}{2\pi RC} \quad (12)$$

According to this equation, the peak frequency is inversely proportional to the capacitance of the geometrical capacitor. Compared to the observed shift in the  $f_{max}$  toward the lower frequency region, the TBAu-B sample achieved the highest capacitance, recommending it to be used in designing electrical double-layer capacitors (EDLCs). Further, this shift is a clear indication of the small contribution of grain boundary to the electrical conduction mechanism within the TB host matrix. This performance is attributed to the rotation of the dipoles, which support the capacitive nature of the existing composite film over resistive behavior and gives it valuable comparative advantages over other composites.

### 3.7 Electrical conduction behavior

Based on the above analyses and their findings, it is found that the TBAu-B sample has achieved the best

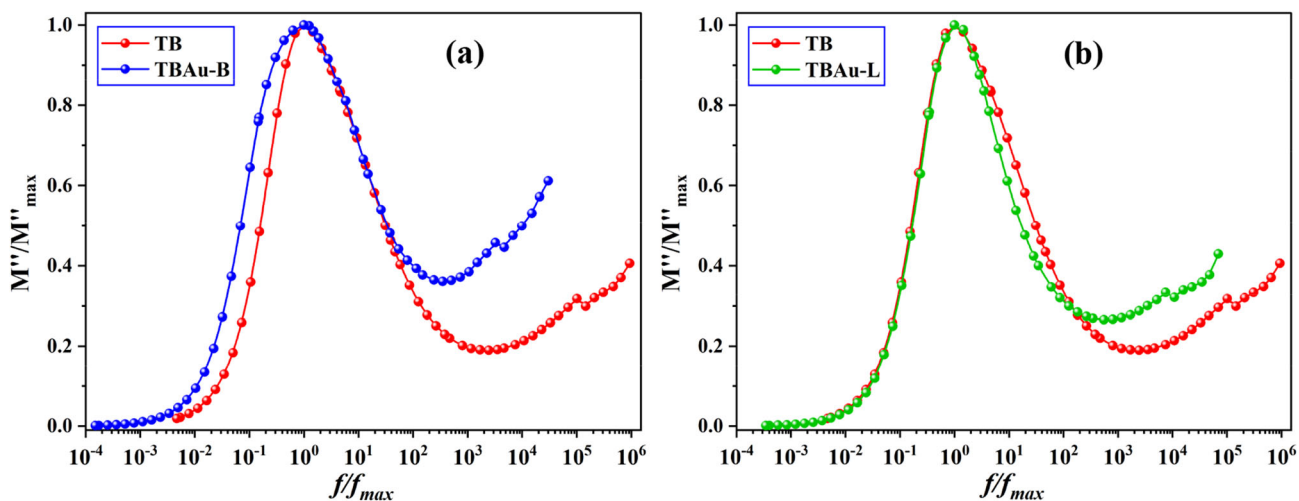


**Fig. 12** The Scaling of  $M''$  curves versus normalized frequency ( $f/f_{max}$ ) of **a** TBAu-B, and **b** TBAu-L nanocomposites compared to the TB curve

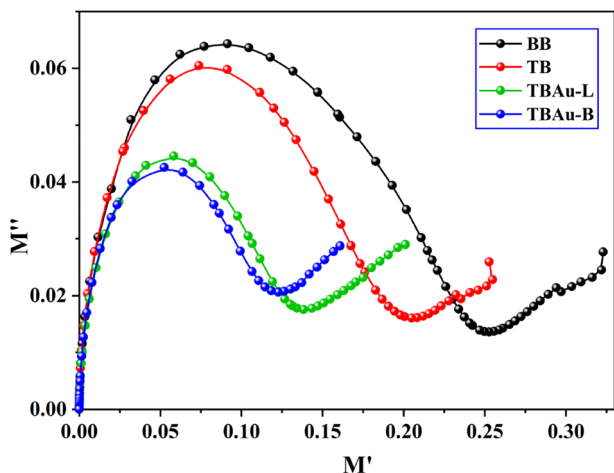


**Fig. 13** The variation of  $M''$  versus  $M'$  (Cole–Cole plot that represents Argand diagrams) for the synthesized samples

results. So, the real ( $\sigma'$ ) and imaginary ( $\sigma''$ ) parts of the electrical conductivity have been carefully studied with varying frequency and temperature, as displayed in Fig. 14.

The complex electrical conductivity ( $\sigma^*$ ) is expressed by the following relation [47]:

$$\sigma^* = \sigma' - i\sigma'' = \frac{\delta}{\pi r^2 R} - i2\pi f \epsilon_0 \left(1 - \frac{C}{C_0}\right) \quad (13)$$

where  $C_0$  symbolizes the capacitance of the capacitor containing free space, while  $C$  is the capacitance of the capacitor containing the TBAu-B sample,  $r$  is the radius of the used electrode, and  $\delta$  is the distance between the two conducting electrodes.

The biosynthesized Au-NPs increased the electrical conductivity, where AuNPs increase the percentage of amorphous sections over crystalline areas, consequently facilitating the transition of excited electrons with short-range distances.

In other words, the relaxation of charge carriers by bouncing back and forth across the localized spots resulted in increased electrical conductivity reported at high frequencies (dispersive region). This improvement is attributed to a shift in the hopping of electrons from long to short-range displacement. The AC electrical conductivity reached  $1.58 \times 10^{-3}$  S/cm at room temperature, as in Fig. 14a. Irfan et al. [48] concluded that the best value for AC electrical conductivity was  $9.03 \times 10^{-4}$  S/cm for PVP/PVA/ 10 wt% NaF at room temperature. Their results promote our TBAu-B nanocomposite as a good candidate for use in the design of energy storage devices and optoelectronic applications.

The DC conductivity ( $\sigma_{dc}$ ) part is represented by a frequency-independent plateau in the  $\sigma'$  curves at lower frequencies. The continuous increase in frequency resulted in the observed enhancement in  $\sigma'$  and produced the dispersive region. The  $\sigma_{dc}$  values of the TBAu-B at different temperatures have been determined from the frequency-independent region and are listed in Table 4.

Further, the  $\sigma'$  values are enhanced with applied temperatures so that the acquired thermal energy induced electrons inside the TBAu-B nanocomposite matrix to hop between localized sites. The rise of temperature paves the way for a transition of small

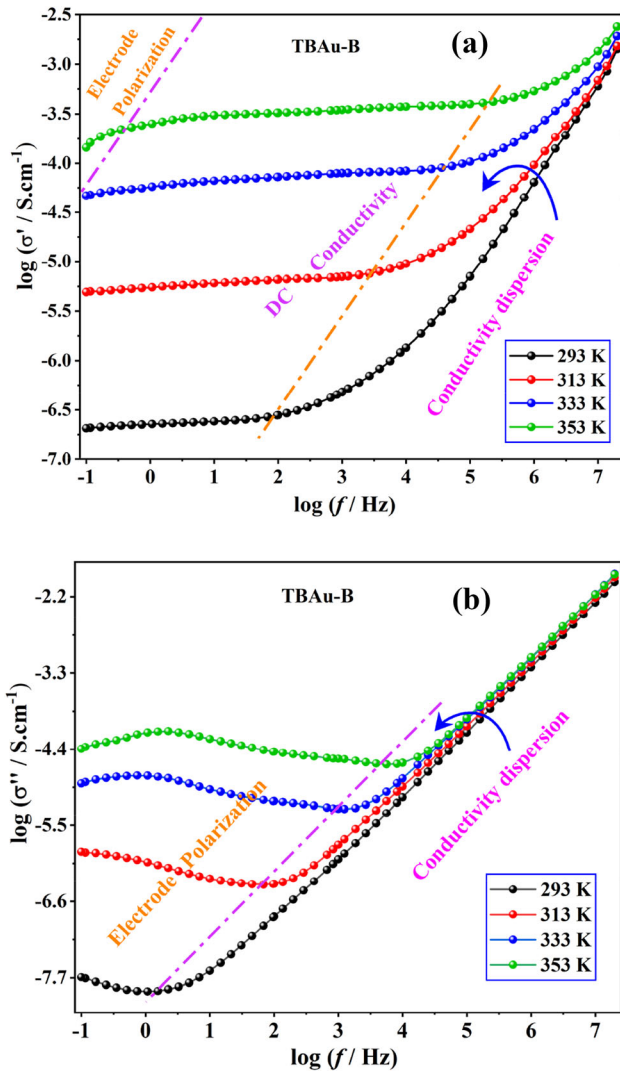


**Fig. 14** The variation of frequency and temperature with **a** real ( $\sigma'$ ), and **b** imaginary ( $\sigma''$ ) parts of the electrical conductivity for the TBAu-B nanocomposite sample

**Table 4** The DC conductivity values ( $\sigma_{dc}$ ) of the TBAu-B at different temperatures determined from the frequency-independent region and the frequency exponent (S)

Temperature (K)	$\sigma_{dc}$ (S/cm)	S
293	$2.09 \times 10^{-7}$	$0.96 \pm 0.09$
313	$5.01 \times 10^{-6}$	$0.78 \pm 0.021$
333	$4.79 \times 10^{-5}$	$0.62 \pm 0.029$
353	$1.62 \times 10^{-4}$	$0.45 \pm 0.03$

polarons with the support of a phonon-assisted tunneling mechanism. This finding proves that the SPE doped with biosynthesized AuNPs has beneficial properties, indicating that it is a suitable basis

material for manufacturing innovative energy storage systems and polymer-based batteries.

It is observed from Fig. 14 that the frequency region corresponding to the electrode polarization effect has significantly increased with temperature, and that both the two conductivity parts follow the universal power law at the high-frequency region. The power law is given by

$$\sigma'_{ac} = \sigma_{dc} + \beta\omega^S \tag{14}$$

where  $\beta$  is a temperature-dependent factor and  $S$  is an exponent related to frequency. The translational movement of the generated electrons influences the  $S$  values, implying that these electrons have relaxed during the electrical conduction process within the (PVP/PVA/CMC)/AuNPs nanocomposites.

The  $S$  values for the TBAu-B sample were calculated in the temperature range 293–353 K and are listed in Table 4. The observed decrease in  $S$  values as the temperature rises indicates that the correlated barrier hopping (CBH) model is the best fit for understanding and characterizing the behavior of conduction electrons throughout the conduction process within the TBAu-B nanocomposite sample, confirming the above findings.

### 4 Conclusion

Plant extract and laser ablation techniques were used to synthesize Au-NPs, whereas the solution casting technique was exploited to prepare the TB/Au-NPs nanocomposites. The reported films' microstructures, morphologies, dielectric characteristics, and optical properties were meticulously investigated using FT-IR, UV-Vis, TEM, and SEM. Additional to the XRD data, the asymmetrical single relaxation peak caused by the dipolar relaxation of the polymeric segments corroborated the semicrystalline character of the TB-based samples. The relaxation time has reduced from  $10^{-3}$  S to  $10^{-4}$  S. The difference between Au-NPs and the TB blend aided in forming small micro-capacitors inside the matrix, hence improving the final product's applicability. The sample with biosynthesized Au-NPs has achieved DC electrical conductivity of  $2.09 \times 10^{-7}$  S/cm at room temperature, which is enhanced to  $1.62 \times 10^{-4}$  S/cm with increasing temperature to 353 K. This alteration led to a considerable rise in AC conductivity values ( $1.58 \times 10^{-3}$  S/cm). Utilizing the leaves' extract produced well-

uniformed distributed Au-NPs, reducing the free areas within the host matrix. The decrease in interatomic distances increases the refractive index with an enhancement in optical properties. These results promote the TBAu-B and TBAu-L nanocomposites for use in some industrial applications in the optoelectronic sector and as a suitable foundation material in developing promising energy storage devices.

## Author contributions

AYY contributed toward resources, data curation, methodology, validation, formal analysis, investigation, conceptualization, writing—original draft, review, and editing.

## Funding

Open access funding provided by The Science, Technology & Innovation Funding Authority (STDF) in cooperation with The Egyptian Knowledge Bank (EKB). The author has not disclosed any funding.

## Data availability

All data generated or analyzed during this study are included in this article and are available with the author.

## Declarations

**Conflict of interest** The author declare that I have no known competing financial interests or personal relationships that could have appeared to influence the work reported in this paper.

**Open Access** This article is licensed under a Creative Commons Attribution 4.0 International License, which permits use, sharing, adaptation, distribution and reproduction in any medium or format, as long as you give appropriate credit to the original author(s) and the source, provide a link to the Creative Commons licence, and indicate if changes were made. The images or other third party material in this article are included in the article's Creative Commons licence, unless indicated otherwise in a credit line to

the material. If material is not included in the article's Creative Commons licence and your intended use is not permitted by statutory regulation or exceeds the permitted use, you will need to obtain permission directly from the copyright holder. To view a copy of this licence, visit <http://creativecommons.org/licenses/by/4.0/>.

## References

1. Y. Liu, D. Sun, S. Askari, J. Patel, M. Macias-Montero, S. Mitra, R. Zhang, W.F. Lin, D. Mariotti, P. Maguire, Enhanced dispersion of TiO<sub>2</sub> nanoparticles in a TiO<sub>2</sub>/PEDOT:PSS hybrid nanocomposite via plasma-liquid interactions. *Sci. Rep.* **5**, 15765 (2015)
2. R.J. Sengwa, P. Dhatarwal, Nanofiller concentration-dependent appreciably tailorable and multifunctional properties of (PVP/PVA)/SnO<sub>2</sub> nanocomposites for advanced flexible device technologies. *J. Mater. Sci. Mater. Electron.* **32**, 9661–9674 (2021)
3. A.M. Abdelghany, A.H. Oraby, M.O. Farea, Influence of green synthesized gold nanoparticles on the structural, optical, electrical and dielectric properties of (PVP/SA) blend. *Physica B* **560**, 162–173 (2019)
4. A.Y. Yassin, A.M. Abdelghany, M.M. Shaban, Y.M. Abdallah, Synthesis, characterization and electrochemical behavior for API 5L X70 carbon steel in 5% sulfamic acid medium using PVP/PEMA blend filled with gold nanoparticles. *Coll. Surf. A* **635**, 128115 (2022)
5. D. Zhang, M. Wang, A.G. Brolo, J. Shen, X. Li, S. Huang, Enhanced performance of dye-sensitized solar cells using gold nanoparticles modified fluorine tin oxide electrodes. *J. Phys. D* **46**, 024005 (2012)
6. P.M. Tiwari, K. Vig, V.A. Dennis, S.R. Singh, Functionalized gold nanoparticles and their biomedical applications. *Nanomaterials* **1**, 31–63 (2011)
7. S. Alex, A. Tiwari, Functionalized gold nanoparticles: synthesis, properties and applications—a review. *J. Nanosci. Nanotechnol.* **15**, 1869–1894 (2015)
8. E.M. Abdelrazek, I.S. Elashmawi, A. El-Khodary, A. Yassin, Structural, optical, thermal and electrical studies on PVA/PVP blends filled with lithium bromide. *Curr. Appl. Phys.* **10**, 607–613 (2010)
9. F.M. Ali, R.M. Kershi, Synthesis and characterization of La<sup>3+</sup> ions incorporated (PVA/PVP) polymer composite films for optoelectronics devices. *J. Mater. Sci. Mater. Electron.* **31**, 2557–2566 (2020)



10. I.S. Elashmawi, E.M. Abdelrazek, A.Y. Yassin, Influence of  $\text{NiCl}_2/\text{CdCl}_2$  as mixed filler on structural, thermal and electrical properties of PVA/PVP blend. *Br. J. Appl. Sci. Technol.* **4**, 4263–4279 (2014)
11. V. Parameswaran, N. Nallamuthu, P. Devendran, A. Manikandan, E.R. Nagarajan, Assimilation of  $\text{NH}_4\text{Br}$  in polyvinyl alcohol/poly(N-vinyl pyrrolidone) polymer blend-based electrolyte and its effect on ionic conductivity. *J. Nanosci. Nanotechnol.* **18**, 3944–3953 (2018)
12. R. Alipour, A. Khorshidi, A.F. Shojaei, F. Mashayekhi, M.J. Moghaddam, Skin wound healing acceleration by Ag nanoparticles embedded in PVA/PVP/Pectin/Mafenide acetate composite nanofibers. *Polym. Test.* **79**, 106022 (2019)
13. E.A. Takara, S.V. Pereira, M.L. Scala-Benuzzi, M.A. Fernández-Baldo, J. Raba, G.A. Messina, Novel electrochemical sensing platform based on a nanocomposite of PVA/PVP/RGO applied to IgG anti-Toxoplasma gondii antibodies quantitation. *Talanta* **195**, 699–705 (2019)
14. A.Y. Yassin, Dielectric spectroscopy characterization of relaxation in composite based on (PVA–PVP) blend for nickel–cadmium batteries. *J. Mater. Sci. Mater. Electron.* **31**, 19447–19463 (2020)
15. A.Y. Yassin, Impedance, structural and thermal analyses of polyvinyl alcohol/polyvinyl pyrrolidone blend incorporated with  $\text{Li}^+$  ions for lithium-ion batteries. *J. Mater. Res. Technol.* **15**, 754–767 (2021)
16. N.M. Deghiedy, S.M. El-Sayed, Evaluation of the structural and optical characters of PVA/PVP blended films. *Opt. Mater.* **100**, 109667 (2020)
17. G. Veena, B. Lobo, Microstructural features, spectroscopic study and thermal analysis of potassium permanganate filled PVA–PVP blend films. *J. Phys. Condens. Matter.* **33**, 255101 (2021)
18. H. Huang, P. He, N. Hu, Y. Zeng, Electrochemical and electrocatalytic properties of myoglobin and hemoglobin incorporated in carboxymethyl cellulose films. *Bioelectrochemistry* **61**, 29–38 (2003)
19. M.P. Adinugraha, D.W. Marseno, Synthesis and characterization of sodium carboxymethylcellulose from cavendish banana pseudo stem (*Musa cavendishii* LAMBERT). *Carbohydr. Polym.* **62**, 164–169 (2005)
20. S.K. Abdel-Aal, M.F. Kandeel, A.F. El-Sherif, A.S. Abdel-Rahman, Synthesis, characterization, and optical properties of new organic-inorganic hybrid perovskites  $[(\text{NH}_3)_2(\text{CH}_2)_3]\text{-CuCl}_4$  and  $[(\text{NH}_3)_2(\text{CH}_2)_4]\text{CuCl}_2\text{Br}_2$ . *Phys. Status Solidi A* **218**, 2100036 (2021)
21. S.K. Abdel-Aal, A.S. Abdel-Rahman, Graphene influence on the structure, magnetic, and optical properties of rare-earth perovskite. *J. Nanoparticle Res.* **22**(9), 1 (2020)
22. S.K. Abdel-Aal, A.I. Beskrovnyi, A.M. Ionov, R.N. Mozchil, A.S. Abdel-Rahman, Structure investigation by neutron diffraction and x-ray diffraction of graphene nanocomposite  $\text{CuO-rGO}$  prepared by low-cost method. *Phys. Status Solidi A* **218**, 2100138 (2021)
23. T.M. Gunathilake, Y.C. Ching, C.H. Chuah, N.D. Hai, L. Nai-Shang, Electro-stimulated release of poorly water-soluble drug from poly (Lactic Acid)/carboxymethyl cellulose/ZnO nanocomposite film. *Pharm. Res.* **37**, 1–20 (2020)
24. M.M. Coleman, D.J. Skrovanek, J. Hu, P.C. Painter, Hydrogen bonding in polymer blends. I. FTIR studies of urethane-ether blends. *Macromolecules* **21**, 59–65 (1988)
25. J.C. Cuevas, J. Heurich, F. Pauly, W. Wenzel, G. Schön, Theoretical description of the electrical conduction in atomic and molecular junctions. *Nanotechnology* **14**, R29 (2003)
26. S.K. Abdel-Aal, A.S. Abdel-Rahman, W.M. Gamal, M. Abdel-Kader, H.S. Ayoub, A.F. El-Sherif, M.F. Kandeel, S. Bozhko, E.E. Yakimov, E.B. Yakimov, Crystal structure, vibrational spectroscopy and optical properties of a one-dimensional organic-inorganic hybrid perovskite of  $[\text{NH}_3\text{CH}_2\text{CH}(\text{NH}_3)\text{CH}_2]\text{BiCl}_5$ . *Acta. Crystallogr. B* **75**(5), 880–886 (2019)
27. A.Y. Yassin, A.M. Abdelghany, Synthesis and thermal stability, electrical conductivity and dielectric spectroscopic studies of poly (ethylene-co-vinyl alcohol)/graphene oxide nanocomposite. *Phys. B* **608**, 412730 (2021)
28. R.J. Sengwa, S. Choudhary, P. Dhatarwal, Nonlinear optical and dielectric properties of  $\text{TiO}_2$  nanoparticles incorporated PEO/PVP blend matrix based multifunctional polymer nanocomposites. *J. Mater. Sci. Mater. Electron.* **30**, 12275–12294 (2019)
29. J.A. Elegbede, A. Lateef, M.A. Azeez, T.B. Asafa, T.A. Yekeen, I.C. Oladipo, D.A. Aina, L.S. Beukes, E.B. Gueguim-Kana, Biofabrication of gold nanoparticles using xylanases through valorization of corn cob by *Aspergillus niger* and *Trichoderma longibrachiatum*: antimicrobial, antioxidant, anticoagulant and thrombolytic activities. *Waste Biomass Valoriz.* **11**, 781–791 (2020)
30. S.K. Abdel-Aal, A.S. Abdel-Rahman, Fascinating physical properties of 2D hybrid perovskite  $[(\text{NH}_3)(\text{CH}_2)_7(-\text{NH}_3)]\text{CuCl}_x\text{Br}_{4-x}$ ,  $x = 0, 2$  and  $4$ . *J. Electron. Mater.* **48**(3), 1686–1693 (2019)
31. Y.H. Elbasha, A.E. Omran, S.M. Hussien, M.A. Mohamed, R.A. Ibrahim, W.A. Rashidy, A.S. AbdelRahaman, H.H. Hassan, Molecular and spectroscopic analysis of zinc oxide doped sodium phosphate glass. *Nonlinear Opt. Quantum Opt.* **52**, 337–347 (2020)
32. Y.H. Elbasha, S.M. Hussien, J. Khaliel, M.A. Mohamed, A.E. Omran, R.A. Ibrahim, W.A. Rashidy, A.S. AbdelRahaman, H.H. Hassan, Infrared spectroscopic analysis of

- cadmium doped sodium zinc phosphate glass matrix. *Non-linear Opt. Quantum. Opt.* **54**, 105–114 (2021)
33. A.M. Salem, A.R. Mohamed, A.M. Abdelghany, A.Y. Yassin, Effect of polypyrrole on structural, optical and thermal properties of CMC-based blends for optoelectronic applications. *Opt. Mater.* **134**, 113128 (2022)
  34. A.Y. Yassin, A.R. Mohamed, E.M. Abdelrazek, M.A. Morsi, A.M. Abdelghany, Structural investigation and enhancement of optical, electrical and thermal properties of poly(vinyl chloride-co-vinyl acetate-co-2-hydroxypropyl acrylate)/graphene oxide nanocomposites. *J. Mater. Res. Technol.* **8**, 1111–1120 (2019)
  35. J.D. Dow, D. Redfield, Toward a unified theory of Urbach's rule and exponential absorption edges. *Phys. Rev. B* **5**, 594–610 (1972)
  36. J.G. Mei, S.M. Yu, J. Cheng, Heterogeneous catalytic wet peroxide oxidation of phenol over delaminated Fe–Ti-PILC employing microwave irradiation. *Catal. Commun.* **5**, 437–440 (2004)
  37. Z.K. Heiba, A.M. El-naggar, M.B. Mohamed, A.M. Kamal, M.M. Osman, A.A. Albassam, G. Lakshminarayana, The effect of concentration of nano CdS/Fe prepared under different conditions on the structural, optical absorption and linear/nonlinear parameters of PVA/PVP polymer blend. *Opt. Mater.* **122**, 111788 (2021)
  38. M. Abdelaziz, Optical and dielectric properties of poly(vinyl acetate)/lead oxide composites. *J. Mater. Sci. Mater. Electron.* **23**, 1378–1386 (2012)
  39. A.Y. Yassin, A.R. Mohamed, A.M. Abdelghany, E.M. Abdelrazek, Enhancement of dielectric properties and AC electrical conductivity of nanocomposite using poly (vinyl chloride-co-vinyl acetate-co-2-hydroxypropyl acrylate) filled with graphene oxide. *J. Mater. Sci. Mater. Electron.* **29**, 15931–15945 (2018)
  40. J. Zhu, H. Gu, Z. Luo, N. Haldolaarachige, D.P. Young, S. Wei, Z. Guo, Carbon nanostructure-derived polyaniline metamaterials: electrical, dielectric, and giant magnetoresistive properties. *Langmuir* **28**, 10246–10255 (2012)
  41. A. Arya, A.L. Sharma, Effect of salt concentration on dielectric properties of Li-ion conducting blend polymer electrolytes. *J. Mater. Sci. Mater. Electron.* **29**, 17903–17920 (2018)
  42. M. Sadiq, M.M.H. Raza, A.K. Singh, S.K. Chaurasia, M. Zulfeqar, A. Arya, J. Ali, Dielectric properties and ac conductivity behavior of rGO incorporated PVP-PVA blended polymer nanocomposites films. *Mater. Today Proc.* **49**, 3164–3169 (2022)
  43. P. Dhatarwal, R.J. Sengwa, Tunable  $\beta$ -phase crystals, degree of crystallinity, and dielectric properties of three-phase PVDF/PEO/SiO<sub>2</sub> hybrid polymer nanocomposites. *Mater. Res. Bull.* **129**, 110901 (2020)
  44. V. Siva, D. Vanitha, A. Murugan, A. Shameem, S.A. Bahadur, Studies on structural and dielectric behaviour of PVA/PVP/SnO nanocomposites. *Compos. Commun.* **23**, 100597 (2021)
  45. R. Dutta, A. Kumar, Dielectric relaxation dynamics and AC conductivity scaling of metal-organic framework (MOF-5) based polymer electrolyte nanocomposites incorporated with ionic liquid. *J. Phys. D* **50**, 425302–425312 (2017)
  46. S. Rani, N. Ahlawat, R. Punia, K.M. Sangwan, P. Khandelwal, Dielectric and impedance studies of La and Zn co-doped complex perovskite CaCu<sub>3</sub>Ti<sub>4</sub>O<sub>12</sub> ceramic. *Ceram. Int.* **44**, 23125–23136 (2018)
  47. V. Saltas, D. Pentari, F. Vallianatos, Complex electrical conductivity of biotite and muscovite micas at elevated temperatures: a comparative study. *Materials* **13**, 3513 (2020)
  48. M. Irfan, A. Manjunath, S.S. Mahesh, R. Somashekar, T. Demappa, Influence of NaF salt doping on electrical and optical properties of PVA/PVP polymer blend electrolyte films for battery application. *J. Mater. Sci. Mater. Electron.* **32**, 5520–5537 (2021)

**Publisher's Note** Springer Nature remains neutral with regard to jurisdictional claims in published maps and institutional affiliations.